Non-Newtonian rheology of crystal-bearing magmas and implications for magma ascent dynamics

Luca Caricchi [a,*], Luigi Burlini [a], Peter Ulmer [a], Taras Gerya [a],
Melissa Vassalli [b,c], Paolo Papale [b]

[a] *Department of Earth Sciences, ETH Zurich, Clausiusstrasse 25, CH-8092, Zurich, Switzerland*
[b] *Istituto Nazionale di Geofisica e Vulcanologia, Via della Faggiola 32, 56126 Pisa, Italy*
[c] *Physics Department, Università di Bologna, Via Berti Pichat 6/2, 40127 Bologna, Italy*

Abstract

The eruptive dynamics of volcanic systems are largely controlled by the viscosity of deforming magma. Here we report the results of a series of high-temperature, high-pressure experiments at conditions relevant for volcanic conduits (250 MPa confining pressure and temperature between 500 °C and 900 °C) that were undertaken to investigate the rheology of magma with crystal fractions varying between 0.5 and 0.8 (50 to 80 wt.%) at different strain-rate conditions. The experiments demonstrate that the presence of crystals increases the relative viscosity (ratio between the viscosity of the mixture and the viscosity of the melt phase) of magmas and additionally induces a decrease of the relative viscosity with increasing strain-rate (shear thinning, non-Newtonian behavior). The experimental results, combined with existing data at low crystal fractions (0–0.3), were used to develop a semi-empirical parameterization that describes the variations of relative viscosity for crystal fractions between 0 and 0.8 and accounts for the complex non-Newtonian rheology of crystal-bearing magmas.

The new parameterization, included into numerical models simulating the magma ascent dynamics, reveals that strain-rate-dependent rheology significantly modifies the dynamic behavior inside volcanic conduits, particularly affecting the magma fragmentation conditions.
© 2007 Elsevier B.V. All rights reserved.

Keywords: magma rheology; experimental deformation; non-Newtonian rheology; conduit-flow dynamics; fragmentation

1. Introduction

The volcanic eruption dynamics are intimately related to the rheological behavior of magma (Dingwell, 1996). The knowledge of the rheology of such materials is therefore prerequisite for volcanic hazard assessment, as it directly contributes to the eruptive behavior of volcanic systems. Magma consists of a mixture of a silicic liquid, crystals and gases and the flow behavior of magmatic mixtures is ultimately determined by the presence of these different components. While magmas have been extensively investigated with respect to the solubility of gases, viscosity of the melt fraction and the rheological effect of gas bubbles (e.g. Webb and Dingwell, 1990; Lejeune et al.,

---

* Corresponding author. Tel.: +41 44 632 78 24; fax: +41 44 632 16 36.
E-mail address: luca.caricchi@erdw.ethz.ch (L. Caricchi).

1998; Llewellin and Manga, 2005; Papale et al., 2006), an equation able to account for the influence of crystals on magma rheology is still unavailable. The simplifying assumption of pseudo-fluid Newtonian behavior (viscosity not depending on strain-rate, $\dot{\gamma}$) implemented in numerical models designed to simulate volcanic eruption (Melnik and Sparks, 1999; Papale, 1999; Melnik, 2000), could indeed induce significant errors in the estimation of the flow dynamics inside the conduit.

We have, therefore, conducted a series of experiments on a water bearing (2.7 wt.% H_2O) rhyolitic melt containing quartz particles, which closely represents a magma rising inside a volcanic conduit, employing different crystal fractions, temperature and strain rate conditions to study potential non-Newtonian effects related to the presence of crystals. Our experimental results are combined with literature data obtained for low solid-fraction materials (Thomas, 1965) and used to constrain a system of equations that account for the variations of η_r (ratio between the viscosity of the mixture and the viscosity of the suspending liquid phase) over a wide range of crystal fractions ϕ (0–0.8) and strain-rates (10^{-7}–$10^{0.5}$ s^{-1}). By introducing these equations in the numerical model described by Papale (2001), which considers the variations of the physical properties of magma during flow in the volcanic conduit (e.g. decompression induced exsolution of volatiles, variations of densities, presence of bubbles in the mixture), the effect of crystals on the conduit dynamics of magmas can adequately be quantified.

The new set of equations provides two principal advances for volcanic eruption modeling: (1) the possibility to simulate eruptions of crystal-rich magmas ($\phi > 0.4$) that are characteristic of highly explosive eruptions, such as for example the eruptions of the Fish Canyon Tuff (Bachmann et al., 2002), the 1631 BC eruption of Mount Vesuvius (Rosi et al., 1993) or the 1991 eruption of Pinatubo (Rutherford et al., 1993). In the past, it was very difficult to perform appropriate simulations of these volcanic eruptions due to the lack of equations describing η_r of magmas containing such high crystal volume fractions. (2) In addition, the new set of equation provides an adequate description of the complex $\dot{\gamma}$-dependent rheology of natural magmas that can now be taken into account in numerical simulations of magma flow dynamics.

2. Experimental procedure

2.1. Sample preparation

Powdered oxides and hydroxides were thoroughly mixed to obtain a fine-grained powder of haplogranitic composition (Online material, Table 1), containing 2.7 wt.%

H_2O added as $AlO(OH)$ and $Al(OH)_3$. These two hydroxides were mixed in appropriate proportions to balance the Al_2O_3 and H_2O content of the glass. The powdered mixture was melted for 24 hours in a large volume-internally heated pressure vessel at 1100 °C and 180 MPa, producing approximately 1 kg of homogeneous glass (confirmed by electron microprobe analysis, Online material, Table 1). The H_2O content of the glass was verified after synthesis by FTIR (Fourier Transform infrared spectroscopy) at LMU-University of Munich and resulted 2.7±0.1 wt.% H_2O. The equilibrated glass was subsequently ground to a very fine grain-size powder (2–4 μm) and mixed with appropriate proportions of crushed quartz to obtain the desired crystal fractions (ϕ). The quartz particles were sieved and the grain size class between 65 and 125 μm was selected. The mixtures of particles and glass were subsequently hot-isostatically pressed (HIP) at 250 MPa and 800 °C for 1 h to re-melt the glass and remove the porosity. Cylindrical specimens of about 1.8 cm^3 were drilled from the hot pressed material. The chemically and texturally homogeneous material contained neither visible gas bubbles nor crystal-clusters. The particular compositions of starting materials were selected because the viscosity of the melt phase is well known (e.g. Hess and Dingwell, 1996) and the system is chemically very stable. The very steep slope of the quartz–liquidus surface in the ternary quartz–albite–orthoclase system for the pressure–temperature range investigated minimizes the amount of reactions between melt and suspended quartz-grains during the course of the deformation experiments. Electron microprobe analyses of the glasses conducted before and after the experiments with duration between 1 and 6 h, revealed insignificant variations in glass composition ($\Delta SiO_2 = -0.09$, $\Delta Al_2O_3 = +0.16$, $\Delta Na_2O = -0.37$, $\Delta K_2O = -+0.31$; all within standard deviation of multiple analyses; Online material, Table 1). For the purposes of this work, chemical stability of the investigated system is fundamental because it allows rigorous control on the degree of crystallinity and on the viscosity of the suspending liquid. Chemical reaction would produce variations in the degree of crystallinity and in the viscosity of the liquid, thereby inducing significant errors in the resulting values of η_r. For these reasons we favored synthetic samples over natural materials. The viscosities of the haplogranitic melt at different temperatures were estimated using the equations reported in (Hess and Dingwell, 1996) and (Giordano et al., 2007).

2.2. Experimental methods and apparatus

All experiments were conducted in a high-temperature, high-pressure internally heated Paterson-type deformation

Table 1
Summary of results of deformation experiments at 250 MPa confining pressure

Experiment number	n	Gamma	Torque (Nm)	Shear stress (MPa)	Shear strain rate (s^{-1})	Log η_{app} (Pa s)	Log η_r (Pa s)	Logη_r / Log$\eta_{r(Newtonian)}$
$\phi=0.5$ $T=500$ °C $\tau_0=90.6$ MPa								
PO770	1	0.04	7.1	36.45	3.12E-06	13.07	2.60	0.92
PO770	1	0.05	12.2	62.40	6.12E-06	13.01	2.59	0.92
PO751	1	0.15	15.6	79.61	4.92E-06	13.21	2.63	0.98
PO751	1	0.17	17.3	87.98	7.79E-06	13.05	2.47	0.92
PO751	1	0.14	18.6	94.63	1.14E-05	12.92	2.34	0.87
PO751	2	0.14	23.6	100.19	2.07E-05	12.68	2.10	0.78
PO751	2	0.22	25.5	108.36	2.71E-05	12.60	2.02	0.75
PO751	2	0.43	32.8	139.36	6.21E-05	12.35	1.77	0.66
$\phi=0.6$ $T=600$ °C $\tau_0=20.9$ MPa								
PO674	1	0.010	1.7	5.01	4.76E-06	12.02	3.50	0.91
PO674	1	0.02	3.2	9.39	8.97E-06	12.02	3.50	0.91
PO674	2	0.06	5.0	14.82	3.09E-05	11.68	3.08	0.80
PO674	2	0.07	6.0	17.58	6.28E-05	11.45	2.85	0.74
PO674	2	0.011	6.9	20.38	9.43E-05	11.33	2.74	0.71
PO674	2	0.16	6.5	19.08	9.14E-05	11.32	2.72	0.71
PO674 c	*4*	*0.167*	*"*	*27.54*	*4.25E-04*	*10.81*	*2.29*	*0.60*
PO674 c	*4*	*0.335*	*"*	*38.46*	*8.84E-04*	*10.64*	*2.12*	*0.55*
$\phi=0.7$ $T=800$ °C $\tau_0=86.9$ MPa								
PO670	1	0.02	5.0	14.61	5.12E-06	12.46	6.59	1.04
PO670	1	0.04	7.9	23.32	8.68E-06	12.43	6.57	1.04
PO670	3	0.1	15.5	38.08	2.52E-05	12.18	6.32	1.00
PO670	3	0.15	20.8	50.98	4.64E-05	12.04	6.18	0.97
PO670	3	0.190	22.6	55.89	5.25E-05	12.03	6.16	0.97
PO670 c	*4*	*0.162*	*"*	*84.62*	*1.25E-04*	*11.83*	*5.97*	*0.94*
PO670 c	*4*	*0.243*	*"*	*108.71*	*3.24E-04*	*11.53*	*5.66*	*0.89*
PO670 c	*4*	*0.399*	*"*	*117.18*	*6.77E-04*	*11.24*	*5.38*	*0.85*
$\phi=0.7$ $T=850$ °C $\tau_0=38.4$ MPa								
PO669	1	0.02	4.2	12.45	5.01E-06	12.40	7.01	0.99
PO669	1	0.06	9.2	27.08	9.19E-06	12.47	7.09	1.00
PO669	3	0.15	13.6	33.46	2.98E-05	12.05	6.67	0.94
PO669	3	0.19	15.6	38.24	6.06E-05	11.80	6.42	0.90
PO669	3	0.24	16.9	41.50	9.33E-05	11.65	6.27	0.88
PO669 c	*4*	*0.080*	*"*	*39.50*	*6.03E-05*	*11.82*	*6.43*	*0.91*
PO669 c	*4*	*0.093*	*"*	*48.48*	*1.65E-04*	*11.47*	*6.09*	*0.86*
PO669 c	*4*	*0.119*	*"*	*54.17*	*4.44E-04*	*11.09*	*5.70*	*0.80*
$\phi=0.8$ $T=850$ °C $\tau_0=110.7$ MPa								
PO673	3	0.05	20.7	86.69	5.55E-06	13.19	7.81	0.97
PO663	3	0.07	24.5	105.37	8.25E-06	13.11	7.72	0.96
PO673	4	0.06	23.9	100.10	9.21E-06	13.04	7.65	0.95
PO673	4	0.080	26.9	112.66	3.17E-05	12.55	7.15	0.89
PO673	4	0.1	28.8	120.53	6.40E-05	12.27	6.87	0.85
PO673 c	*4*	*0.208*	*"*	*120.16*	*1.11E-04*	*12.03*	*6.65*	*0.82*
PO673 c	*4*	*0.212*	*"*	*123.83*	*1.76E-04*	*11.85*	*6.47*	*0.80*
PO673 c	*4*	*0.222*	*"*	*135.82*	*4.70E-04*	*11.46*	*6.08*	*0.75*
$\phi=0.8$ $T=900$ °C $\tau_s=79.7$ MPa								
PO672	3	0.11	18.2	78.18	8.82E-06	12.95	7.91	0.89
PO660	3	0.230	19.1	82.09	2.59E-05	12.50	7.54	0.85
PO660	3	0.26	22.6	96.94	5.27E-05	12.26	7.30	0.82
PO660	3	0.28	23.6	101.52	7.94E-05	12.11	7.15	0.80
PO660 c	*4*	*0.503*	*"*	*104.01*	*1.35E-04*	*11.89*	*6.93*	*0.78*

The data presented in italics are values converted from compression experiments according to Eqs. (38–42) (Paterson and Olgaard, 2000); τ_0 is the fictive yield strength obtained by extrapolating the stress–strain rate curves at high shear strain rate to zero strain rate; the maximum strain attained in these experiments (gamma) is the shear strain rate calculated in torsion multiplied by the duration of the experiment in seconds. Abbreviations: n=stress exponent; gamma=maximum strain; log η_{app}=logarithm of the apparent viscosity; log η_r=logarithm of the relative viscosity; logη_r/log$\eta_{r(Newtonian)}$=the ratio of the logarithms of the relative viscosity at a given strain rate divided by the logarithm of the relative viscosity in the Newtonian field, i.e. at very low strain rate. The definitions of the apparent and relative viscosities are given in the text.

apparatus (Paterson and Olgaard, 2000) at 250 MPa confining pressure and temperatures varying between 500 and 900 °C. The sample diameter for all experiments was 12 mm; the sample length varied between 4 and 5 mm in torsion and between 12 and 15 mm in uniaxial compression tests. The cylindrical specimens are placed between alumina cylinders that transmit the differential stress on the sample. The assembly is composed of 4 alumina cylinders, 2 on each side used to transmit the differential stress to the sample, and two alumina spacers that are used to separate the transmitting cylinders from direct contact with the partially molten sample. Temperature is measured by a shielded K-type (Chromel–Alumel) thermocouple at the top of the upper spacer that is 3 mm thick. The temperature difference along the entire sample length does not exceed 2 K. The entire sample assembly is inserted in an iron tube in order to isolate the sample from the confining argon gas. The resolution of the load cell is 1 Nm in torsion (Paterson and Olgaard, 2000; Barnhoorn et al., 2004) and 1 kN in compression, which induces uncertainties in reported stress values of 3 MPa and 5 MPa respectively (Table 1).

2.3. Carrying out the deformation experiments

Torsion and compression experiments were performed at constant strain-rates (Fig. 1) that varied between $1 \cdot 10^{-6}$ and $1 \cdot 10^{-4}$ s^{-1} in torsion and up to $1 \cdot 10^{-3}$ s^{-1} in compression configuration. In the case of torsion experiments, the relation between torque (applied force given by the reading of the internal load cell of the apparatus) and stress is dependent on the stress exponent (n) of the material under investigation (Paterson and Olgaard, 2000). In the experiments reported here, the n-values for comparable ranges of strain rate were similar for all crystal fractions (Table 1; Fig. 1 Online material). The appropriate n values required to convert the torque in stress were selected from logarithmic plots displaying the maximum torque versus strain rate. In such a plot the slopes of the fitting lines for different torque values correspond to the stress exponent (Fig. 1 Online material). Total strain reached up to gamma 0.8 in torsion (shear strain Paterson and Olgaard, 2000) and 20% shortening in compression configuration. Two to three deformation tests were performed for each different degree of solid fractions (0.5, 0.6, 0.7 and 0.8) to investigate the effect of variable temperatures and to cover a wide range of strain rates.

Several experiments were repeated at the same strain-rate to evaluate the reproducibility in peak stress that resulted within 5 MPa (e.g. Fig. 1, $\phi = 0.6$, $T = 600$ °C) that converts to an average error in viscosity of about 0.05 log

units. Stepping strain rate tests, i.e. increasing the strain rate in a stepwise manner, were only conducted after steady state stress conditions were achieved for a given strain rate (Fig. 1a). The stress values presented in Table 1 are corrected for the strength of the iron jacket applying the flow law reported by Frost and Ashby (1982) that is in accordance with calibrations performed in our laboratory by Barnhoorn et al. (2004), and that is also favored by Rutter et al. (2006). This correction results in a decrease of the viscosities between 0.2 and 0.01 log units compared to the raw data for the lowest and the highest stresses measured respectively. The presence of the iron jacket and the resolution of the load cell allow accurate measurements of the viscosity for values higher than 10^9 Pa s. In fact, an applied stress of 3 MPa corresponding to the resolution of the internal load cell in torsion configuration at $1 \cdot 10^{-3}$ s^{-1} shear rate, results an apparent viscosity of $10^{9.5}$ Pa s. In order to obtain viscosities larger than 10^9 Pa s for all our samples, the temperatures of the experiments had to be adjusted as a function of the solid fraction (500 °C for $\phi = 0.5$, 600 °C for $\phi = 0.6$, 850 °C for $\phi = 0.7$ and 900 °C for $\phi = 0.8$). In order to compare strain rates and stresses from torsion and compression experiments, uniaxial strain rate and stress values were converted to shear strain-rates and shear stresses using the conversion laws 38–42 reported in (Paterson and Olgaard, 2000). Compression and torsion experiments performed at similar strain rate, ϕ and temperature compare well in terms of peak stresses (e.g at $\phi = 0.7$ and $T = 850$ °C, Fig. 1).

3. Experimental results

All torsion and compression experiments exhibit identical behavior of an initial linear increase of stress with strain (elastic behavior), followed by a yielding stage and finally flow at a constant value of stress (Fig. 1a). The elastic response of the sample was restricted to a relatively short interval of strain, followed by longer, progressively decreasing strain-hardening (stress increase with respect to strain) until flow at constant stress was attained. The strain-hardening phase extended over a larger strain interval in torsion than in compression tests for comparable strain rates (e.g. at $\phi = 0.7$ and $T = 850$ °C, Fig. 1a). Values reported in Table 1 represent the maximum stress attained for the applied strain-rate during the flow stage. The stress and strain rate values were used to calculate the apparent viscosity (Eq. 1):

$$\eta_{app} = \tau / \dot{\gamma} \qquad (1)$$

where τ is the peak shear stress and $\dot{\gamma}$ is the corresponding shear rate (Fig. 1b).
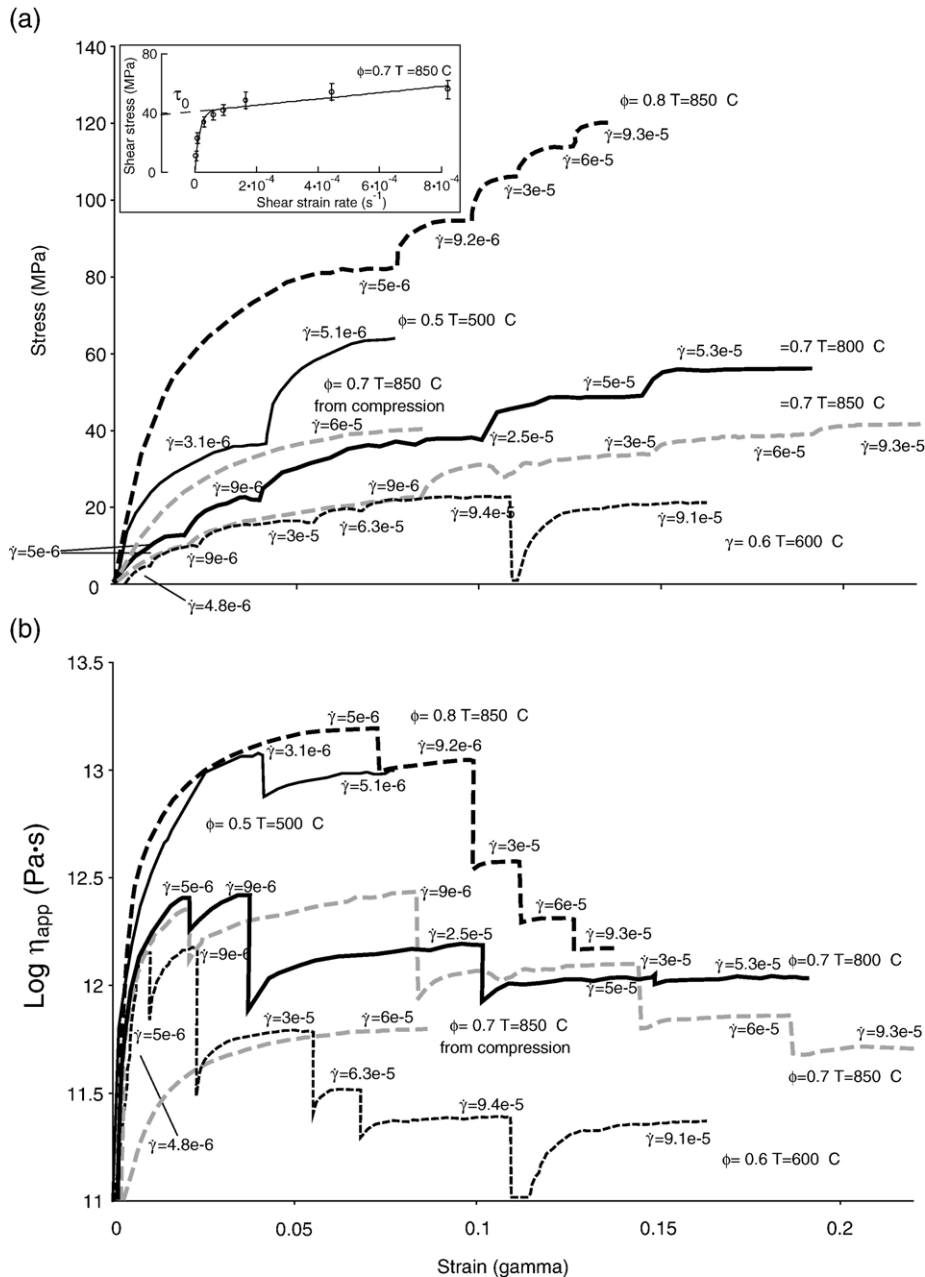
Fig. 1. Selected examples of experiments performed in torsion and compression configuration at 250 MPa confining pressure. The relevant conditions for each experiment (crystal fraction (ϕ), temperature and strain rates ($\dot{\gamma}$) in s^{-1} are indicated as labels attached to each curve. a) Recorded stress values plotted against strain. The steps in the individual curves represent the increase of stress due to an increase of strain rate during the experiments (i.e. strain rate stepping experiments, for details see text). The Inset illustrates the fitting procedure performed to obtain the apparent viscosity with respect to the strain rate applying Eq. (4). The data represent the maximum stress reached during the flow of the material for each strain rate. The stress values tend to decrease to zero at zero strain rate testifying the absence of yield strength. The"fictive yield strength" (τ_0, Table 1; see text for more details) is obtained by extrapolation of the stress values at relatively high strain rate ($>10^{-4}$ s^{-1}) to zero strain rate (dashed line). b) Calculated apparent viscosities obtained from individual strain rates ($\eta_{app} = \tau/\dot{\gamma}$) plotted versus strain. Increasing the strain rate for any given crystal fraction (ϕ) and temperature induces a decrease of viscosity interpreted as shear thinning behavior.

In order to test if strain could affect the rheology of the investigated material, we performed several experiments (e.g. $\phi = 0.6$ and $T = 600$ °C; Fig. 1a and b) where

the sample was unloaded after a series of strain stepping tests and subsequently reloaded applying a previously used strain rate. No variations were observed in the peak

stress and thus in the resulting viscosity of the material ([Fig. 1](#)a and b) testifying to the absence of thixotropic behavior (variation of viscosity with the increase of applied strain).

3.1. Effect of temperature

The strength of the samples decreased with increasing temperature ([Fig. 1](#)a, $\phi=0.7$ $T=850$ °C and $T=800$ °C): a 50 °C temperature increase leads to a decrease of the viscosity of approximately 0.2 log units. However, the same temperature increase results in a viscosity decrease of 0.4 log units for the pure melt phase (Hess and Dingwell, 1996; Giordano et al., 2007). This difference indicates that for such high crystal fractions the rheological behavior of the system is controlled by both, the viscosity of the melt and the interactions between the suspended particles.

3.2. Effect of crystal fraction

The effect of the crystal fraction can be evaluated by comparing the stresses and apparent viscosities of experiments performed on samples with $\phi=0.7$ and

0.8 at 850 °C temperature ([Fig. 1](#) a): an increase of the solid fraction by 0.1 induces a considerable increase in the peak stress values, which results in an increase of the apparent viscosity of 0.6–0.7 log units ([Fig. 1](#)a and b, [Table 1](#)). In order to separate the effects of temperature and the effects of crystal fraction on the viscosity we plot the relative viscosity (η_r) of the samples for the different solid fractions ([Fig. 2](#)). The relative viscosity is given as:

$$\eta_r = \eta_{app}/\eta_{melt} \qquad (2)$$

where η_{app} is the measured apparent viscosity of the sample and η_{melt} is the viscosity of the suspending melt phase at a given temperature. η_r is therefore independent of temperature, because the change in temperature induces only a change in the viscosity of the suspending melt that is implicitly included in the definition of the relative viscosity. The increase of suspended solid fraction produces an increase of the relative viscosity ([Fig. 2](#)) that is particularly dependent on solid fraction between $\phi=0.5$ and $\phi=0.7$. The ϕ where viscosity starts to increase exponentially is defined as the "maximum packing fraction" of the system (ϕ_{max};
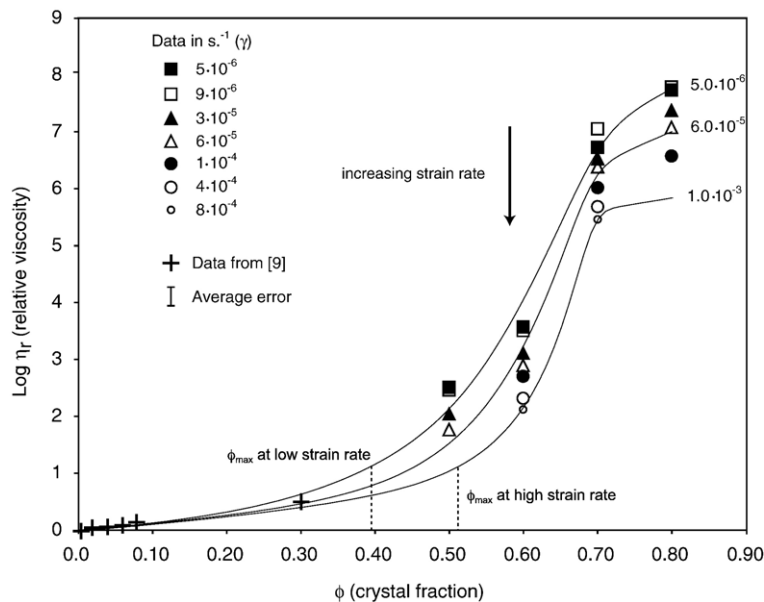

Fig. 2. Logarithmic values of relative viscosity (η_r) as a function of solid fraction (ϕ). Symbols represent experimental data from this study except the black crosses that are data taken from literature (Thomas, 1965). The average error in relative viscosity indicated by a bar on the diagram represents the uncertainty of the calculated viscosities based on repeat experiments performed with the same crystal fractions at different temperature and considering the differences in the calculated viscosities of the suspending liquids using the algorithms provided by (Hess and Dingwell, 1996) and (Giordano et al., 2007). Continuous lines represent calculated η_r obtained from Eqs. (3), (6)–(9) and a viscosity of the suspending melt phase calculated with algorithm provided by (Hess and Dingwell, 1996). The relative viscosities (η_r) increases non-linearly with increasing suspended solid fraction. ϕ_{max} corresponds to the onset of the exponential increase of η_r and increases with increasing $\dot{\gamma}$ as indicated by the vertical, broken lines for low and high strain rates respectively.

Krieger, 1972). This parameter is dependent on several factor related to crystal size, shape, distribution and orientation (Chong et al., 1971; Garboczi et al., 1995; Saar et al., 2001). The lines displayed in Fig. 2 represent the results of the fitting procedure outlined in detail in Section 5.

3.3. Effect of strain rate

In all experiments viscosity was independent from strain rate for values lower than 10^{-5} s^{-1} i.e. Newtonian behavior was observed (Fig. 1b). Above this threshold, an increase of strain rate always induced a decrease of viscosity (Fig. 1b); this behavior is defined as "shear thinning" (e.g. Webb and Dingwell, 1990) and is an expression of non-Newtonian behavior. Note that shear thinning results in an increase of ϕ_{max} (Fig. 2) with increasing strain rate.

The effects of strain rate on the relative viscosity are highlighted in Fig. 3a.

The magnitude of decrease of relative viscosity is directly proportional to ϕ. Fig. 3b displays the logarithmic value of η_r (relative viscosity) for any given value of strain rate normalized to the logarithmic value of η_r at low strain rates (i.e. in the Newtonian field). This normalization allows evaluation of the relative effects of shear thinning on the relative viscosity. Fig. 3a and b reveal that the *absolute magnitude of decrease* of the relative viscosity is higher for the higher crystal fractions, whereas the *relative decrease* of η_r is higher for lower crystal fractions of $\phi = 0.5$ and $\phi = 0.6$.

The principal experimental results can be summarized as follows:

1. In all experiments flow at constant value of stress and absence of strain weakening was observed.
2. Strain did not influence the rheology of the samples implying the absence of thixotropic behavior.
3. The relative viscosity (η_r) increased by about 5 orders of magnitude with increasing solid fractions (quartz crystals) from 0.5 to 0.8 (Fig. 2).
4. Two different dependencies of apparent viscosity from the strain-rate corresponding to Newtonian and non-Newtonian behavior (Fig. 3a and b) were observed. The Newtonian regime is characteristic for low strain-rates and the apparent viscosity in this regime is independent of the strain-rate (although it depends on solid fraction). In the non-Newtonian regime the apparent viscosity decreases with increasing strain-rate (shear thinning behavior).
5. The absolute magnitude of the apparent viscosity decrease is larger for larger solid fractions (Fig. 3a).

However, the relative magnitude (i.e. log η_r/ log$\eta_{r(Newtonian)}$ of the shear thinning-induced decrease of viscosity is larger for lower solid fractions ($\phi = 0.5$ to $\phi = 0.6$, Fig. 3b).

The experiments, thus, imply that the introduction of solid particles into a viscous liquid results in two principal rheological effects: (i) increase of relative viscosity of the suspension with increasing solid fraction, and (ii) the enhancement of non-Newtonian behavior.
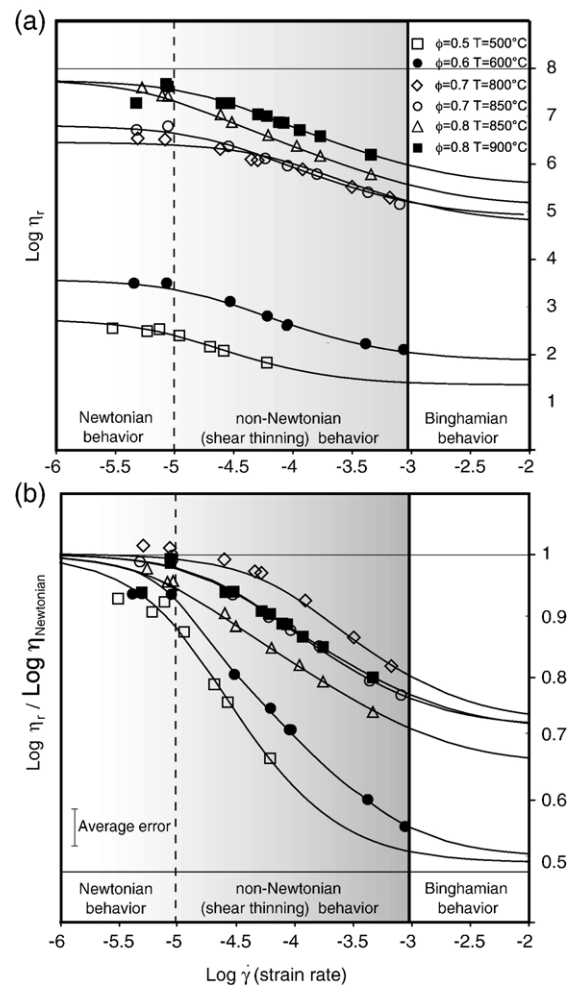

Fig. 3. a) Logarithmic values of relative viscosity (η_r) plotted as a function of the logarithm of the strain-rate ($\dot{\gamma}$, s^{-1}). This diagram illustrates the dependence of η_r on solid fraction and highlights the shear thinning behavior of crystal bearing samples with increasing $\dot{\gamma}$. b) Variation of the logarithmic values of the relative viscosity at a given strain-rate divided by the relative viscosity in the Newtonian region (Logη_r/Log$\eta_{r(Newtonian)}$, i.e. at very low strain-rates) as a function of the logarithm of the strain rate. Details of the experiments are provided in Table 1.
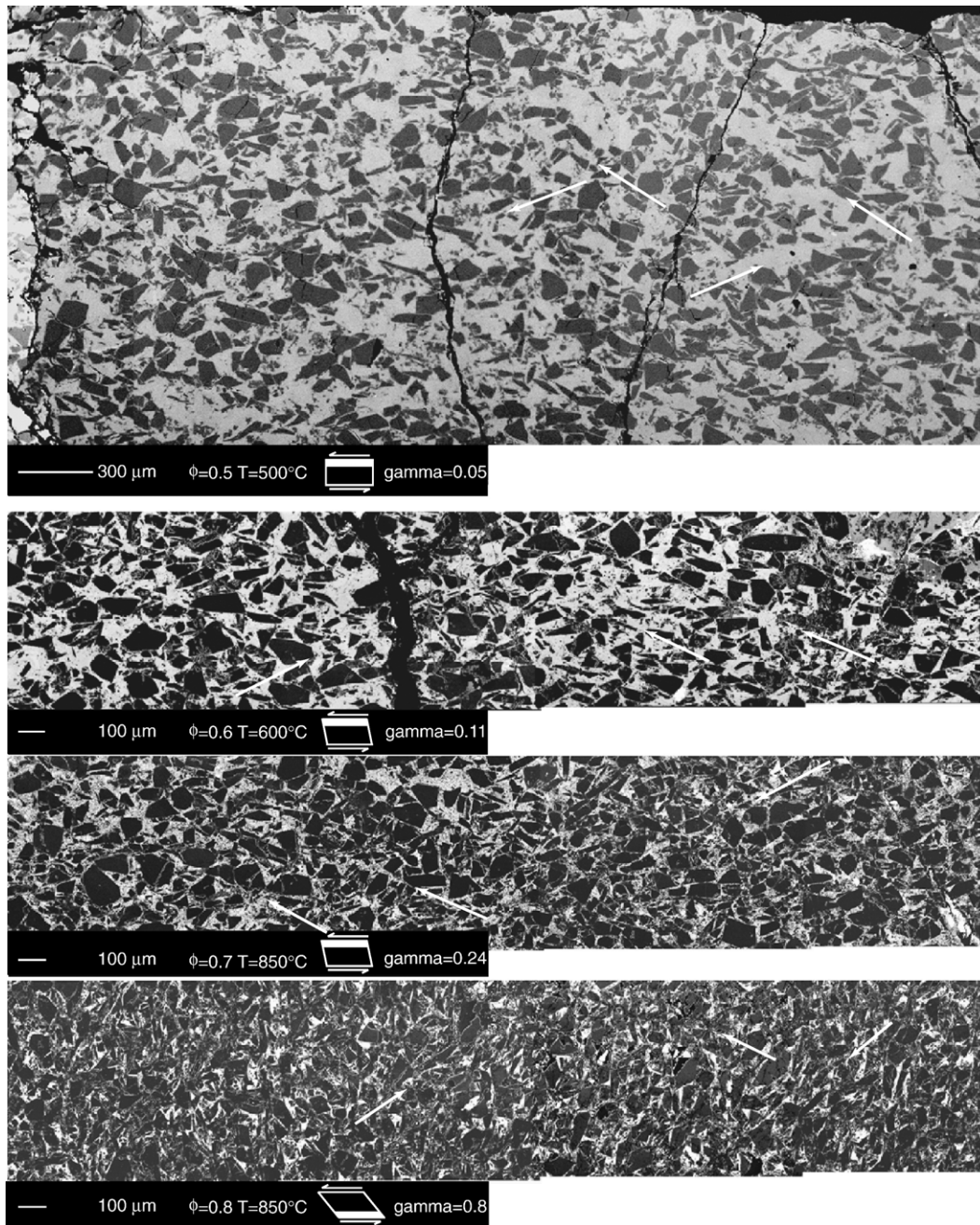
Fig. 4. Back scattered electron (BSE) images of recovered, deformed samples. The glass phase is light grey and the quartz particles are dark grey. For each individual image, a scale bar, the crystal fraction (ϕ), the experimental temperature, a sketch of the orientation of the applied stress field, and the total applied strain are indicated in the lower left corner. The white bars drawn in the sketched samples indicate the portions of the samples where the images were taken. The arrows in the BSE images indicate the strain localization bands. The localization bands are oriented at around 30 and 150° with respect to the direction of flow in all samples regardless of the solid fraction and total applied strain.

3.4. Microstructures

The microstructures generated during the deformation experiments were analyzed by back scattered electron (BSE) imaging of polished sections cut through the recovered, deformed samples (Fig. 4). Investigated samples from torsion experiments were cut out from the external portion of the specimens, with the short axis

parallel to the cylinder axis, where simple shear geometry is best appreciated and shear is maximal (Paterson and Olgaard, 2000). Samples deformed in uniaxial compression were cut along the centre, parallel to the cylinder axis. In all experiments (torsion and compression) planar features were observed. However, we concentrate our discussion on the microstructures obtained in torsion experiments, because, for the aspect ratio of the samples deformed in compression (1–1.25), the internal stress is not homogeneously distributed and this renders the interpretation rather complicated (Kulkarni and Kalpakjian, 1969).

The planar features are oriented at about 30° and 150° with respect to the shear plane. These features were observed in all deformed specimens and their geometry is independent of the total strain applied. These bands are highlighted in Fig. 4 by arrows and consist of melt and crystals elongated parallel to the planar structures. The crystals in these clusters have average grain sizes that are smaller than in the rest of the sample. The thickness of these bands appears to correlate inversely with the crystal fraction (i.e. the higher the crystal fraction the thinner the bands).

Comparable planar features have previously been observed in torsion experiments conducted by Holtzman et al. (2005) at higher ϕ (0.94–0.96). They used a viscous energy dissipation function to argue that the minimum of total work required to produce deformation is obtained for angles of the localization bands of 25° with respect to the shear plane.

4. Discussion on the effects of crystals on magma rheology

Previous studies have shown that very different types of solid–liquid suspensions regarding composition (e.g. hard sphere colloidal suspensions or lithium disilicate melt plus lithium disilicate crystals) and fraction of suspended solid particles ($0.1 \leq \phi \leq 0.8$ (Krieger, 1972; Dekruif et al., 1985; Ryerson et al., 1988; Vanderwerff and Dekruif, 1989; Brückner and Deubener, 1997; Deubener and Bruckner, 1997; Sato, 2005; Scott and Kohlstedt, 2006; Rutter et al., 2006) display very similar dependence of the relative viscosity (η_r) on ϕ and $\dot{\gamma}$: the relative viscosity η_r increases with ϕ in a sigmoidal fashion (Fig. 2). With increasing strain rate solid–liquid suspensions can display Newtonian, non-Newtonian and Binghamian behavior (Krieger, 1972; Vanderwerff and Dekruif, 1989; Brückner and Deubener, 1997; Deubener and Bruckner, 1997; Sato, 2005). At relatively low strain rates ($<10^{-5}$ s^{-1}; Brückner and Deubener, 1997; Scott and Kohlstedt, 2006 and from this study;

Fig. 3a and b) the behavior is Newtonian. An increase of strain rate induces shear thinning (non-Newtonian behavior) where the viscosity decreases until a minimum value is reached (Fig. 3). This minimum represents the onset of Binghamian behavior, which is characterized by a viscosity that is lower than the Newtonian viscosity but likewise independent from the strain rate. Here the definition of Binghamian behavior is not strictly related to the presence of yield strength but refers to the independence of the viscosity from the strain rate. In our experiments, the Binghamian behavior was not reached but only approached (Fig. 1a and b) due to the limitation of the maximum strain rates (10^{-3} s^{-1}) attainable. However, the existence of this rheological behavior at high $\dot{\gamma}$ has clearly been demonstrated previously (Krieger, 1972; Dekruif et al., 1985; Vanderwerff and Dekruif, 1989; Brückner and Deubener, 1997; Deubener and Bruckner, 1997). In the Binghamian region a value of "fictive yield strength"(τ_0) can be obtained by linear extrapolation of the flow stress values at high strain rate to zero strain rate (the principle is illustrated in the Inset in Fig. 1a). τ_0 can be associated to the stress value at which macroscopic deformation starts in the material, for this reason it could be interpreted as a yield strength that is strongly dependent on crystal fraction and temperature. The values of fictive yield strength at the conditions of the experiments are reported in Table 1. The flow law results in a linear decrease of stress with decreasing strain rate at high deformation rates ($>10^{-4}$ s^{-1} Binghamian behavior). For intermediate strain rates (10^{-4}–10^{-5} s^{-1} non-Newtonian behavior) the stress decreases exponentially. For strain rates lower than 10^{-5} s^{-1} the stress decreases linearly towards zero (Newtonian behavior) (Inset Fig. 1a).

Viscous heating is unable to account for the large decrease of viscosity (1-2 orders of magnitude) observed in our experiments: The strain rates and the dimensions of the specimens are far too low to induce a substantial production of heat and, consequently, a considerable thermal gradient between the sample and the thermocouple used to control the temperature during the experiments. In case the temperature would rise, the thermocouple would register this temperature increase and the temperature-controller would readjust the power output to bring the temperature immediately back to the target value. Considering the maximum measured viscosity ($\sim 10^{13}$ Pa s) and an applied strain rate of $5 \cdot 10^{-6}$ s^{-1} (e.g. f=0.8; T=850 °C; Table 1), the heat production per unit time would result in $1 \cdot 10^{-2}$ K/s. Taking in account thermal diffusivity for silicic magmas as reported in (Eriksson et al., 2003), viscous heating would not produce any appreciable (0.01 °C) gradient

between the centre of the sample and the thermocouple located at a distance of 8 mm from the center of the sample (5 mm half specimen length and 3 mm spacer). Increasing the strain rate in our experiment to $1 \cdot 10^{-4}$ s^{-1} we observed a decrease of viscosity to 10^{12} Pa s. If we repeat the same calculations, keeping the viscosity constant at the highest observed value of 10^{13} Pa s and applying a strain rate $1 \cdot 10^{-4}$ s^{-1}, this would induce a maximum temperature increase of 3 °C after about 180 s corresponding to a decrease in viscosity of 0.03 log units. For longer periods, the temperature will be constant over the entire sample length and the temperature will be adjusted by the furnace to a constant value of 850 °C.

We would like to emphasize that we have chosen temperature and $\dot{\gamma}$ conditions that keep the melt phase in the "relaxed" Newtonian region (Webb and Dingwell, 1990). For these reasons, the observed shear thinning effects can exclusively be attributed to the presence of the solid quartz particles. This, in turn, implies that the presence of particles induces non-Newtonian behavior in temperature and strain rate ranges where the suspending medium itself behaves Newtonian.

4.1. Flow mechanics of crystal-bearing magmas

The visco-plastic deformation of magmas with ϕ up to 0.8 is due to the flow of the melt phase and consequently the plastic deformation of the suspended particles is negligible (Rosemberg and Handy, 2005; Rutter et al., 2006). This implies that the suspended particles move passively in response to the flow of the melt phase.

In order to understand the mechanics of magma deformation it is fundamental to reconcile the micro-structural observations and the rheological data:

a) It has been demonstrated that the micro-structural ordering (redistribution of melt and crystals) coincides with the transition from Newtonian to shear thinning and finally to Binghamian behavior with increasing strain rate (Fig. 5a) for hard-sphere, relatively diluted, colloidal suspensions and for silicate melt suspensions with $\phi < \phi_{max}$ ($0.1 < \phi < 0.6$; (Dekruif et al., 1985; Vanderwerff and Dekruif, 1989; Brückner and Deubener, 1997; Deubener and Bruckner, 1997; Lyon, 2001; Smith and Zukoski, 2004). In this range of crystal fractions the application of relatively high stress (or high strain rates) leads to the generations of particles aggregates, which align according to the flow directions (Lyon, 2001; Fig. 5a). A lower limit of stress or strain rate has to be overcome before these structures

generate; this threshold corresponds to the transition from Newtonian to non-Newtonian (shear thinning) behavior. The alignment produces a smaller disturbance of the melt flow lines relative to a system that contains randomly distributed particles (Fig. 5a). The occurrence of a viscosity minimum obtained at high strain rates via shear thinning reflects the presence of a Binghamian region that corresponds to the attainment of the maximum or optimum possible ordering in the system (Fig. 5a).

b) For $\phi > \phi_{max}$ the deformation mechanisms are different than far more dilute suspensions because the suspended particles are in reciprocal contact. The flow in such material is, therefore, only possible if a certain amount of dilation occurs, which allows the particles to move relative to each other. The relationships between experimental data and mechanics of deformation for concentrated suspension ($\phi > \phi_{max}$) has been elegantly described by Rutter et al. (2006) in terms of effective mean stress (total mean stress minus melt pressure) and differential stress (Fig. 5b redrawn from Rutter et al., 2006).

At the beginning of our experiments the confining pressure is completely transferred to the melt phase and, consequently, the effective pressure is zero. During the elastic loading of the sample in simple shear experiments the differential stress increases while the effective pressure remains constant at zero because the maximum compressive stress is equal to the tensional stress. Under conditions of pure shear during the elastic loading, the effective mean stress increases by one-third relative to the differential stress, following the no-tension line. This line separates the field of entirely compressive stress on the right hand side from the field of differential stress where at least one tensile component is present on the left hand side (Rutter et al., 2006). The irreversible deformation of the material (yield point, Y or Y^I in Fig. 5b) initiates when the yield surface is encountered. At this point, since all the crystals are in reciprocal contact, a certain amount of dilation has to occur to accommodate the deformation. The dilation induces a decrease of the pore-fluid pressure and, consequently, the effective stress path starts to deviate to the right (Fig. 5b). Differential stress and effective mean stress rise until the critical state line is reached and deformation continues at constant volume, constant differential stress and constant melt pressure (F in Fig. 5b) (Rutter et al., 2006). From the yielding point (Y or Y^I) to the flow at constant differential stress, the evolution of the microstructures induces a certain amount of strain hardening, as observed in our experiments, both in torsion and compression tests (Fig. 1 and 5b). Due to
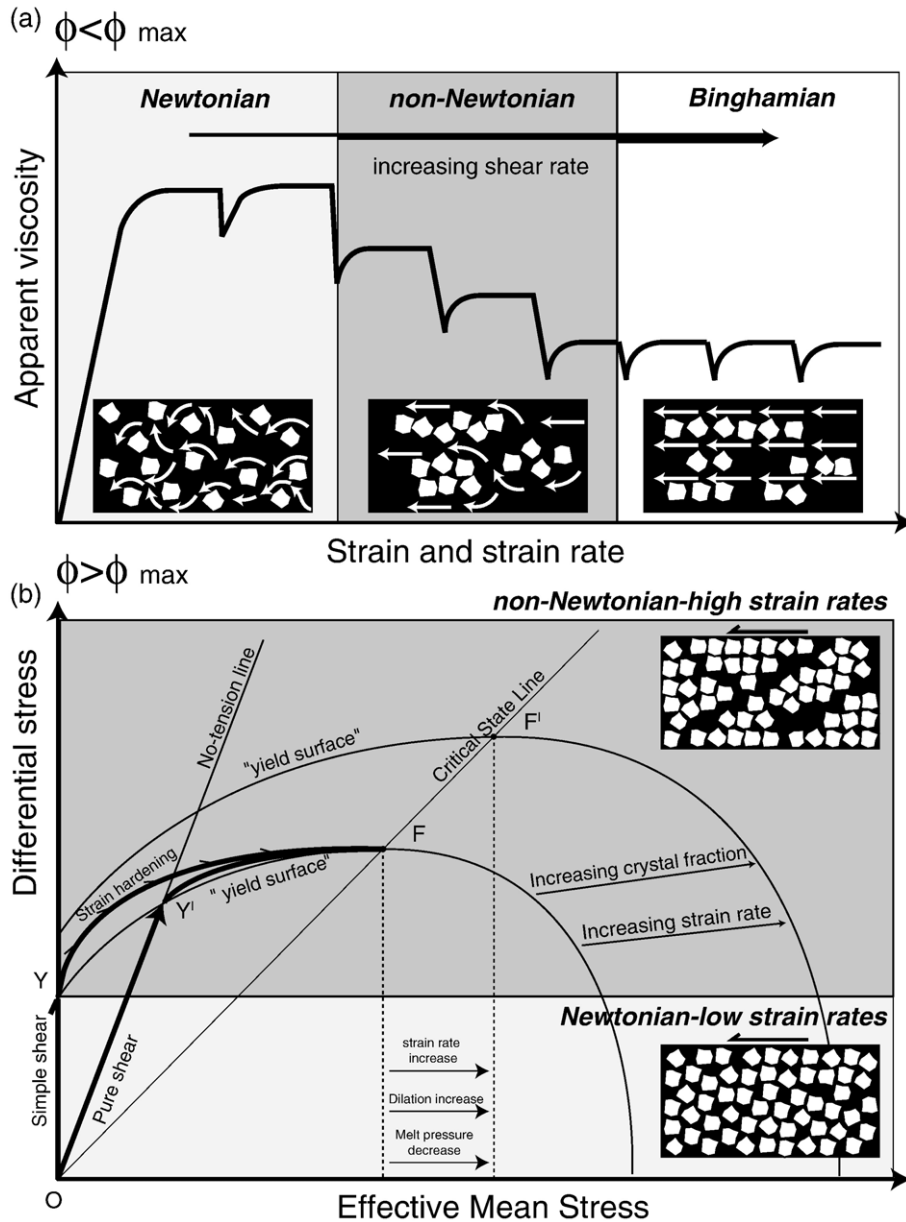
Fig. 5. Diagram illustrating the relationships between observed rheological behavior and microstructures. a) Apparent viscosity plotted against strain. The strain rate increases from the left to the right. In the low strain rate region (left panel) the viscosity does not vary with strain rate corresponding to Newtonian behavior (i.e. viscosity is independent of strain rate). Increase of strain rate first leads to a region of non-Newtonian and ultimately Binghamian behavior (for detailed explanations see text). The pictures inserted in the lower part of the diagram visualize the microstructures generated during the experiments that are responsible for the observed rheological transitions. b) Rheological behavior of crystal bearing magmas in torsion and compression experiments interpreted in terms of differential stress and effective mean stress; Figure redrawn from (Rutter et al., 2006). The paths OY and OY^I represent the loading trajectories for torsion and compression experiments, respectively. At Y or Y^I, depending on the imposed stress field (simple shear or pure shear), the loading path intersects the yielding surface where irreversible deformation of the sample starts. The deformation induces dilation that decreases the melt pressure thereby driving the loading path to the right toward the critical state line. In F, the flow of the material continues at constant differential stress and constant effective mean stress. Increasing crystal fractions or applied strain rates expand the yielding surface; i.e. for material with constant crystal fraction and constant temperature, an increase of strain rate shifts the onset of flow from F to F^I (for more detail see Rutter et al., 2006). The amount of dilation is inversely proportional to the melt pressure and directly proportional to strain rate. Consequently, with increasing strain rate, dilation increases concomitantly with the difference in melt pressure between the yielding point (Y, Y') and the flow (F, F'). The increase of dilation with strain rate promotes the localization features observed in our microstructures, which are responsible for the transition from Newtonian to non-Newtonian behavior. The microstructures corresponding to different rheological behaviors (Newtonian at low strain rates and non-Newtonian at high strain rates) are sketched as inserts on the right hand side of the Figure.

the shape of the yielding surfaces (Rutter et al., 2006) and to the different loading paths followed by simple and pure shear tests, the total strain required to reach flow is less in compression experiments (Figs. 1 and 5 and Table 1).

The dilation that is required to produce flow in the system produces local compaction of the grains (Holtzman et al., 2005), which in turn induces a local increase in the melt pressure. These local pressure gradients force the melt to move relative to the crystals toward regions that are under higher effective pressure (lower melt pressure) where the deformation rates are higher (Rutter et al., 2006). In simple shear experiments the maximum compressive stress is oriented at 45° with respect to the shear plane; compaction is expected to occur at high angle with respect to this component and dilation at low angle.

This process could well be responsible for the generation of crystal and melt-rich bands observed in our experiments, which we consequently interpret as strain localization features. The angle of the localization bands of ±30° reflects minimization of work required to deform the material for such a configuration (Holtzman et al., 2005). Once the melt-enriched bands are established, any further deformation localizes along these zones of weakness (Fig. 5).

The amount of dilation required to reach flow at constant differential stress is a function of both, the crystal fraction and the applied strain rate (F–F^{I} in Fig. 5b). Thus, we infer that in the Newtonian region the melt-pressure gradients (due to local dilation and local compaction) are insufficient to induce significant segregation of melt from crystals. At the onset of shear thinning the strain rate or the stress are high enough to induce the generation of localization bands that facilitate the flow and are responsible for the shear thinning behavior observed in our experiments. Increasing the strain rate increases the melt pressure gradient thereby favoring the segregation of the melt phase from the crystals. This melt-crystal segregation can be envisaged as a reordering of the material, which tends to minimize the energy required for flow. When this reorganization has achieved an optimal configuration, any further increase of strain rate will not lead to an additional decrease of the viscosity; such a micro-structural configuration reflects the attainment and existence of the region of Binghamian behavior at high shear strain rates.

The link between weak, melt-rich zones and the rheological transitions can, in turn, explain the observation that the relative decrease of viscosity due to shear thinning (Log η_{r}/Log$\eta_{\mathrm{r(Newtonian)}}$) is higher for lower crystal fractions (Fig. 1b). In the case of high solid fractions ($\phi = 0.7$ and $\phi = 0.8$), there is an insufficient amounts of melt contained in the localization bands to avoid particles interactions, whereas for solid fraction close to the maximum packing ($\phi = 0.5$ and $\phi = 0.6$), the segregation of melt from crystals is able to produce localization bands with thicknesses that are sufficient to strongly reduce the contacts between the crystals. The substantial reduction of particle interactions produces, therefore, a higher relative decrease of viscosity, with increasing strain rate, compared to the high solid fraction materials.

5. Rheological model

In order to implement the complex rheology of crystal-bearing magmas in numerical codes utilized to simulate conduit flow dynamics, the rheological data obtained from the experiments were mathematically treated with a system of equations that account for both, (i) the increase of the η_{r} with increasing crystal content, and (ii) the decrease of η_{r} with increasing $\dot{\gamma}$. The effect of temperature on the relative viscosity (η_{r}) is implicitly included in the definition of η_{r}, i.e. increasing temperature results in decreasing viscosity of the melt-phase.

The sigmoidal increase of η_{r} as a function of increasing ϕ is described with a modified version of the semi-empirical Eq. (3) given by Costa et al. (2007):

$$\eta_{\mathrm{r}}(\phi) = \frac{1 + \left(\frac{\phi}{\phi_{\max}}\right)^{\delta}}{\left(1 - \alpha \mathrm{erf}\left\{\frac{\sqrt{\pi}}{2\alpha}\frac{\phi}{\phi_{\max}}\left[1 + \left(\frac{\phi}{\phi_{\max}}\right)^{\gamma}\right]\right\}\right)^{B\phi_{\max}}} \quad (3)$$

where α, δ, $\phi_{\max}$ (maximum solid packing fraction), and γ are adjustable parameters. B is the Einstein coefficient that was kept constant during the fitting to its theoretical value of 2.5 (Einstein, 1906).

A continuous trend of η_{app} as a function of $\dot{\gamma}$ was obtained from our stress — strain-rate data by fitting them with a phenomenological flow law that accounts for the $\dot{\gamma}$-dependent rheology of magmatic suspensions (Eq. (4)) as proposed by Brückner and Deubener (1997):

$$\tau(\dot{\gamma}) = m\eta_{\infty 1}\dot{\gamma} + \tau_0 \cdot [1 - \exp(-\dot{\gamma}/\dot{\gamma}_{c1})] \quad (4)$$

where τ is the shear stress, m is a geometrical factor that is equal to 1 in shear experiments, $\eta_{\infty 1}$ is the limiting viscosity at high $\dot{\gamma}$-values prior to the onset of the viscoelastic behavior of the suspending liquid phase, τ_0 is the fictive yield strength (value of shear stress at relatively high strain rates, extrapolated to zero $\dot{\gamma}$; see inset Fig. 1), and $\dot{\gamma}_{c1}$ is the critical $\dot{\gamma}$ where the first non-Newtonian transition takes place. Dividing Eq. (4) by $\dot{\gamma}$ gives the apparent viscosity at each value of $\dot{\gamma}$:

$$\eta_{\mathrm{app}}(\dot{\gamma}) = \eta_{\infty 1} + (\tau_0/\dot{\gamma}) \cdot [1 - \exp(-\dot{\gamma}/\dot{\gamma}_{c1})] \quad (5)$$

The numerical results from the fitting procedure using Eq. (5) and the parameters $\eta_{\infty 1}$, τ_0 and $\dot{\gamma}_{c1}$, are displayed as solid lines in Fig. 3a and b.

5.1. A 3D equation for $\phi - \dot{\gamma}$ dependent viscosity of partially crystallized magmas

In order to describe changes in the relative viscosity (η_r) over the entire range of solid fractions between $0 < \phi \leq 0.8$ the new experimental data produced in this study were combined with literature data obtained at low degrees of solid fraction ($0 < \phi \leq 0.3$) (Thomas, 1965). The crystal-induced shear thinning effects for $\phi \leq 0.3$ are very weak (around $0.1–0.2$ log units) (Ryerson et al., 1988; Sato, 2005) and, thus, for $0 < \phi \leq 0.3$ η_r was assumed to be independent of $\dot{\gamma}$. Using Eq. (5), η_r values were computed for strain rates between 10^{-7} to $10^{-0.5}$ s^{-1}. These relative viscosity data were fitted with Eq. (3) as a function of ϕ at different values of $\dot{\gamma}$ to constrain the variations of the fitting parameters (α, δ, ϕ_{max}, and γ) with respect to $\dot{\gamma}$ (Fig. 2). Variations of the fitting parameters as a function of $\dot{\gamma}$ were then approximated with the following set of equations:

$$\phi_{max} = 0.066499 \cdot \tanh(0.913424) \cdot \log10(\dot{\gamma}) \\ + 3.850623 + 0.591806 \quad (6)$$

$$\delta = -6.301095 \cdot \tanh(0.818496 \cdot \log10(\dot{\gamma}) + 2.86) \\ + 7.462405 \quad (7)$$

$$\alpha = -0.000378 \cdot \tanh(1.148101 \cdot \log_{10}(\dot{\gamma}) + 3.92) \\ + 0.999572 \quad (8)$$

$$\gamma = 3.987815 \cdot \tanh(0.8908 \cdot \log10(\dot{\gamma}) + 3.24) \\ + 5.099645 \quad (9)$$

Calculated relative viscosities obtained from the model (Eqs. (3), (6)–(9)) are compared with our experimental data in Fig. 2.

The combination of Eqs. (3) with (6), (7), (8), and (9) results in a complete (3D) rheological model describing η_r as a function of both, ϕ and $\dot{\gamma}$ (Fig. 6). Incorporating rheological models that describe the viscosity of the suspending liquid phase (e.g. Hess and Dingwell, 1996; Giordano et al., 2007) furthermore allows the prediction of the temperature and strain rate dependence of the apparent magma viscosity. This, in turn, can be used to calculate the dependence of the fictive yield strength (τ_0) on crystal fraction and temperature by fitting the apparent viscosity of the magma as a function of strain rate to Eq. (5).

It is important to note that our experiments only approached the Binghamian field, therefore, an addi-

tional decrease of the viscosity could occur when the strain rate is increased to values higher than 10^{-3} s^{-1} (maximum value reached in our experiments). Furthermore, viscous heating effect could start to play an important role for such high strain rate values and this phenomenon would further decrease the viscosity. These observations imply that for strain rates higher then 10^{-3} s^{-1} our equation only provides an upper limit of viscosity.

The errors of the predicted η_r values as a function of ϕ and $\dot{\gamma}$ were evaluated by using two different models to estimate the viscosity of the pure melt phase (Hess and Dingwell, 1996; Giordano et al., 2007) and by performing experiments at different temperatures but identical crystal fraction, where the only difference was the viscosity of the melt phase. The error on the η_r calculation due to experimental uncertainty, the viscosity of the suspending melt phase, and the fitting procedure amounts to a maximum value of 0.3 log units as illustrated in Fig. 2 by the differences between the experimental values and the curves obtained from the model (Eqs. (3), (6)–(9)).

6. Numerical modeling

6.1. Physical modeling of magma flow

The parameterization for non-Newtonian viscosity of crystal-bearing magmas expressed by Eqs. (3), (6)–(9) was introduced into the numerical code utilized to model multiphase magma ascent (Papale, 2001). The model describes the 1D, steady, isothermal, separated flow of multiphase magma along a cylindrical volcanic conduit. The flowing magma is described as a homogeneous mixture of liquid and solid phases, mechanically interacting with a gas phase. The gas phase is contained in the form of bubbles below the fragmentation level and it is modeled as a continuous phase with dispersed pyroclasts above this level.

The properties of magma depend on the local pressure-composition conditions. Volatile saturation is determined by modeling the non-ideal gas-liquid thermodynamic equilibrium (Papale et al., 2006). Liquid-crystal density is computed with the model given by Lange (1994) and standard mixing rules were applied (as reported in Rosi et al., 1993). Gas density is calculated through the Modified Redlich–Kwong equation provided by Kerrick and Jacobs (1981).

The friction terms in the momentum equations require a description of mixture viscosity. This in turn depends on the flow regime (either bubbly flow below magma fragmentation, or gas-particle flow above it), on
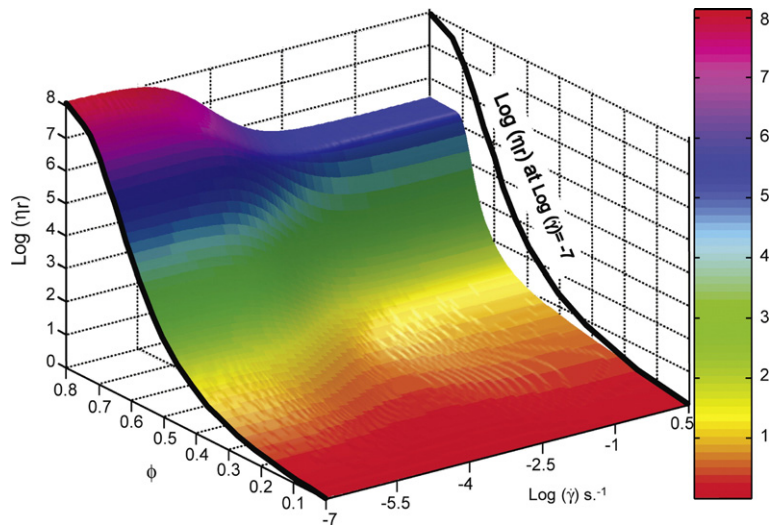
Fig. 6. Variation diagram showing the logarithm of the relative viscosity (log η_r) as a function of crystal fraction (ϕ) and the logarithm of the strain-rate (log $\dot{\gamma}$) (s^{-1}). The η_r values are calculated using Eqs. (3), and (6)–(9). The viscosity of the pure melt phase is computed from the equation reported in (Hess and Dingwell, 1996). The heavy line on the right side depicts the projection of the log η_r at a strain-rate corresponding to 10^{-7} s^{-1} and highlights the influence of $\dot{\gamma}$ on the maximum packing fraction and the shear thinning behavior of crystal bearing magmas.

the viscosity of the continuous phase (liquid magma below fragmentation, gas above it), and on the volume fraction of the dispersed phases (crystals and gas bubbles below fragmentation, pyroclasts above it). Liquid viscosity is modeled through semi-empirical TVF-like equation (Hess and Dingwell, 1996; Romano et al., 2003). Gas bubbles, assumed for simplicity to be undeformable, are accounted for as described in (Papale, 2001). The effects of crystals on the rheology are taken into account by either using the new parameterization presented here (Eqs. (3), (6)–(9)) that includes the effects of non-Newtonian $\dot{\gamma}$-induced decrease in η_{app}, or the simpler Newtonian model proposed by Costa et al. (2007).

6.2. Numerical simulations

The numerical simulations were conducted to evaluate the effects of non-Newtonian behavior of crystal-bearing magmas on the dynamics of magma ascent and fragmentation along volcanic conduits during explosive eruptions. In order to assess the role of high crystal contents and $\dot{\gamma}$-induced decrease of η_{app} of the liquid+crystal homogeneous mixture, we conducted parametric simulations by comparing the results obtained with the present model of suspension rheology with those obtained with the Newtonian model given in (Costa et al., 2007) for crystal-bearing magmas. In order to evaluate the results over a wide spectrum of conditions, we repeated the simulations by determining

the occurrence of magma fragmentation by either the visco-elastic criterion in (Papale, 1999) or the gas bubble overpressure criterion in (Melnik, 2000), and by using two different magmas of rhyolitic and trachytic composition, each with a corresponding typical eruptive temperature. For each set of conditions, the crystal fraction of the erupted magma were let to vary from zero up to $\phi = 0.55$ (relative to the degassed magma). These crystal fractions represent the most interesting range of crystallinity at which the most explosive eruptions occur (e.g. Rosi et al., 1993; Rutherford et al., 1993; Bachmann et al., 2002). Moreover, as the experiments demonstrate, already for $\phi = 0.5$ the non-Newtonian character of magma starts to exert a strong control on the magma viscosity. The highest crystal contents reflect conditions over which numerical convergence is not achieved, due to very high mixture viscosity hence very large gradients of flow variables along the volcanic conduit (Papale, 1999).

6.3. Results of numerical simulations

The numerical results illustrate the effects of incorporating non-Newtonian rheology of crystal-bearing magmas in magma ascent modeling on the dynamics of magma ascent and on the occurrence of magma fragmentation. In addition, these models show the different dynamics associated with the discharge of magmas having different crystal contents. Differences in the calculated magma flow dynamics due to different
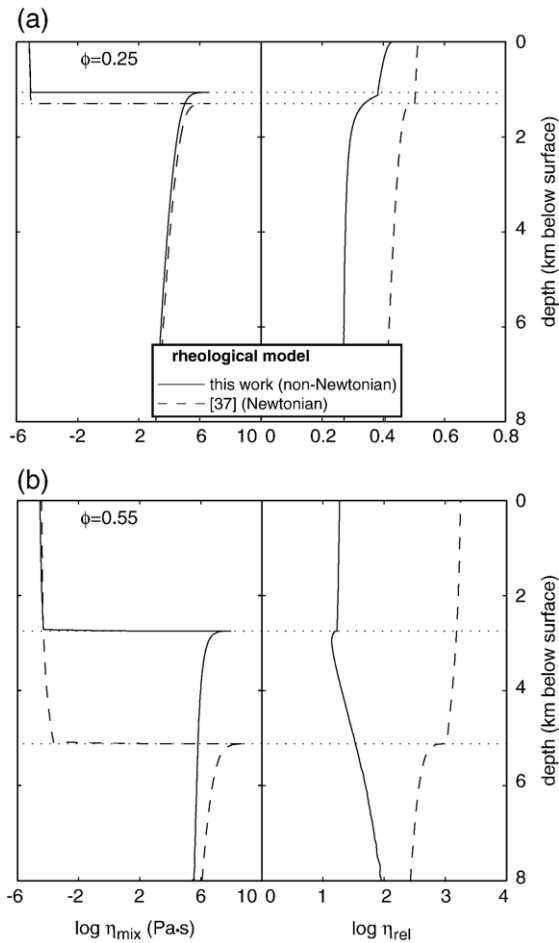
Fig. 7. Diagrams illustrating the results of numerical modeling of volcanic conduit dynamics: computed variations of the logarithm of the viscosity of the mixture (log η_{mix}, left side) and the logarithm of the relative viscosity (log η_r, right side) as a function of depth below the surface for two crystal fractions, a) $\phi=0.25$ and b) $\phi=0.55$, for a trachytic magma (composition given in Romano et al., 2003) with a temperature of 947 °C. The solid and dashed lines refer to the crystal-melt non-Newtonian rheological model presented in this paper and to the Newtonian model given in (Costa et al., 2007), respectively. Calculations reported in this Figure and in Figs. 8 and 9 have been conducted with a conduit length and diameter of 8000 and 50 m, respectively, a stagnation pressure of 200 MPa, 6 wt.% water content (=H_2O-content of the melt phase) and crystal fractions relative to the degassed magma ranging from $\phi=0$ to $\phi=0.55$. Further details of the dynamic conduit model are given in (Papale, 2001).

composition of the liquid magma are not discussed here, since they are the subject of previous work (Papale et al., 1998; Polacci et al., 2004).

Fig. 7 shows the calculated distribution of the mixture viscosity and of η_r along the volcanic conduit for conditions pertaining to trachytic magma; the visco-elastic fragmentation criterion of Papale (1999) has been adopted, and two crystal fractions, $\phi=0.25$ and

$\phi=0=0.25$ (Fig. 7a), the rise of the fragmentation level is only about 250 m and fragmentation occurs for a η_r more than 1 order of magnitude lower than for the case where Newtonian behavior is assumed. With $\phi=0.55$ (Fig. 7b), the uplift of the fragmentation level becomes as large as 2360 m. In this case, the η_r strongly decreases due to non-Newtonian rheology. Contrarily, with Newtonian rheology, the η_r increases approaching fragmentation, reflecting an increase of crystal volume fraction due to density increase of the liquid phase upon degassing. At the level where fragmentation occurs the η_r determined with non-Newtonian rheology is about 2 orders of magnitude lower than for Newtonian rheology.

In spite of the contrasting trends in η_r, the viscosity of the multiphase magma always increases below fragmentation, mainly due to the large effect of H_2O exsolution from the liquid on viscosity (Hess and Dingwell, 1996; Romano et al., 2003; Giordano et al., 2007). Above the magma fragmentation level, the mixture viscosity suddenly decreases by many orders of magnitude approaching that of the continuous gas phase. This is a consequence of the fundamental change in the continuum properties of the magmatic mixture upon fragmentation.
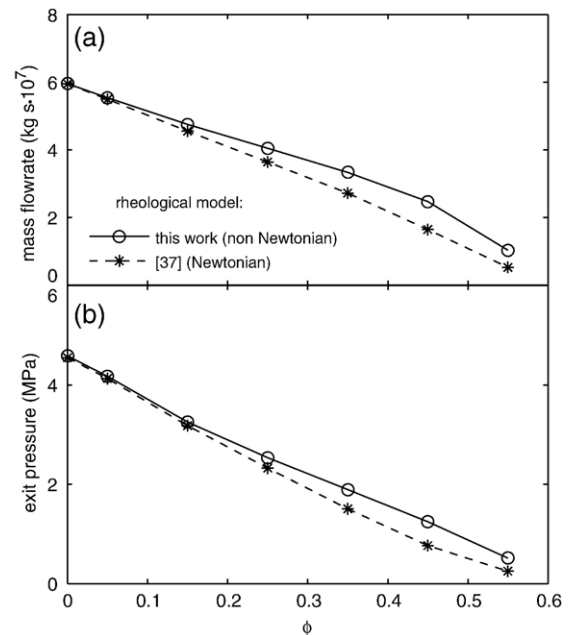

Fig. 8. Diagram illustrating the calculated mass flow rate a) and conduit exit pressure b) as a function of variable crystal fractions of the erupted magma for a trachytic magma (composition given in Romano et al., 2003) with a temperature of 947 °C. The solid lines and circles, and the dashed lines and stars, refer to the crystal-melt systems employing the non-Newtonian rheological model reported in this paper and to the Newtonian model given in (Costa et al., 2007), respectively.

Fig. 8 shows the calculated mass flow-rate and pressure at the conduit exit level obtained for the simulations pertaining to the trachytic magma, the fragmentation criterion as given by Papale (Papale, 1999), and crystal fractions varying from $\phi=0$ to $\phi=0.55$. The numerical results indicate that over the range of crystal contents considered, the mass flow rate decreases by a factor of 6–10 and the exit pressure decreases by about a factor of 10. Non-Newtonian effects tend to reduce mass flow-rates and pressure decreases; these effects vanish when zero crystal content is approached. However, in spite of the large variations in the distribution of magma viscosity (and other flow variables such as gas volume fraction and phase velocities and densities) inside the volcanic conduit in Fig. 7, these quantities change only a small fraction even at large crystal content. Other flow variables (not reported in the Fig. 7) show similar small variations when comparing their values at the conduit exit obtained by either Newtonian or non-Newtonian rheology of the crystal-bearing magma.

Fig. 9 summarizes the conditions calculated at magma fragmentation in terms of depth and magma vesicularity for all simulations performed. In all cases, increasing crystal contents in the discharged magma result in a deepening of the fragmentation level and in a decrease of magma vesicularity at fragmentation. The use of non-Newtonian rheology strongly restricts the range of such variations. As

an example, fragmentation depth and magma vesicularity at fragmentation computed for Newtonian rheology and the fragmentation criterion given by Melnik (2000) amounts to about 6.6 km and 20 vol.% for a trachytic magma. The same quantities become 3.6 km and 50 vol.% when using non-Newtonian rheology. It is remarkable that the overall vesicularity range covered by all the simulations performed with the two fragmentation criteria is largely reduced by the use of non-Newtonian rheology: The total range is <5–90 vol.% with Newtonian rheology and reduced to 40–90 vol.% with non-Newtonian rheology.

7. Conclusions

The experiments reported here demonstrate that the introduction of suspended crystals in a melt phase produces an increase in the relative viscosity η_r and enhances $\dot{\gamma}$-dependent rheology. The shear thinning behavior observed in our experiments is caused by a geometrical redistribution of suspended particles and melt that facilitate the flow of magma resulting in a reduction of viscosity with increasing $\dot{\gamma}$. The generation of melt-enriched bands requires additional, more detailed investigation because these processes could exert strong controls on processes such as the distribution of gas bubble upon volatile exsolution. The coincidence between the maximum applied stress and the direction of the flow
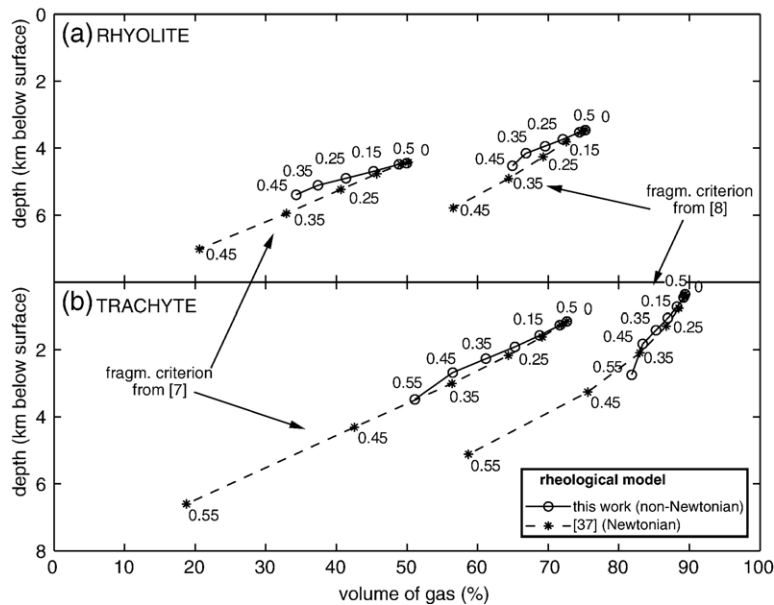

Fig. 9. Diagram illustrating the calculated fragmentation conditions, in terms of depth and magma vesicularity (volume of gas) for a) rhyolitic (reported in Polacci et al., 2004, temperature of 827 °C); and b) trachytic magma compositions (reported in Romano et al., 2003, temperature of 947 °C) for different crystal fractions (=numbers close to the symbols), and different fragmentation criteria according to (Melnik, 2000) and (Papale, 1999). The solid lines and circles, and the dashed lines and stars, refer to the crystal-melt systems employing the non-Newtonian rheological model reported in this paper and to the Newtonian model given in (Costa et al., 2007), respectively.

parallel to the walls in volcanic conduits is optimal to produce melt enriched bands parallel to the flow direction. The alignment of bubbles parallel to the direction of the flow could, in turn, result in a strong effect on magma permeability and consequent exsolution of volatiles during rise from the magma chamber.

The system of Eqs. (3), (6)–(9) presented in this contribution successfully describes the complex rheological behavior of crystal-bearing magmas. These equations provide the basis to evaluate the effects of micro-scale deformation processes occurring during magma flow on the macroscopic behavior of magmas rising inside volcanic conduits during explosive eruptions. The numerical simulations of magma ascent and fragmentation along volcanic conduits infer that the introduction of non-Newtonian rheology of crystal-bearing magma results in large variations in the fragmentation conditions and distribution of flow variables along the conduit. However, the restricted variation of the calculated mass flow-rate and conduit exit conditions do not reflect the large changes observed within the conduit. This is most probably related to the counter-acting effects of reduced η_{app} and increased length of the highly viscous region below fragmentation (Polacci et al., 2004) resulting from the introduction of non-Newtonian rheology. In conclusion, the present results suggest that non-Newtonian behavior significantly affects the internal conduit dynamics and the physical characteristics of magmas at the fragmentation level, while the general eruption dynamics are more sensitive to Newtonian viscosity of the liquid fraction. The introduction of non-Newtonian rheology has the effect of largely decreasing the extent to which crystals, and in general solid particles transported in the magma (e.g. xenoliths or lithics), affect the fragmentation conditions, although the general trend due to increasing amount of crystals does not change. The crystal content of the erupted magma, which resulted to be the magma characteristic that most significantly decreased the vesicularity of the magma at fragmentation, now turns to be much less effective when taking into account non-Newtonian rheology.

Finally, it must be stressed that the present simulations are performed under the simplifying assumption of 1D magma flow. It is likely that other complexities due to non-Newtonian rheology may arise when considering multi-D phenomena. As an example, it may be expected that non-Newtonian rheology plays a significant role in decreasing the local η_{app} close to conduit walls where shear stress concentrates. In such a case, the process of viscous dissipation and local increase of temperature (Costa and Macedonio, 2003, 2005; Vedeneeva et al., 2005) would become important, requiring specific numerical simulations to be performed to evaluate these additional effects.

Appendix A. Supplementary data

Supplementary data associated with this article can be found, in the online version, at doi:10.1016/j.epsl.2007.09.032.

References

Bachmann, O., Dungan, M.A., Lipman, P.W., 2002. The fish canyon magma body, San Juan volcanic field, Colorado: rejuvenation and eruption of an upper-crustal batholith. J. Petrol. 43, 1469–1503.

Barnhoorn, A., Bystricky, M., Burlini, L., Kunze, K., 2004. The role of recrystallization on the deformation behaviour of calcite rocks: large strain in torsion experiments on Carrara marble. J. Struct. Geol. 36, 885–903.

Brückner, R., Deubener, J., 1997. Description and interpretation of the two phase flow behavior of melts with suspended crystals. J. Non-Cryst. Solids 209, 283–291.

Chong, J.S., Christiansen, E.B., Baer, A.D., 1971. Rheology of concentrated suspensions. J. Appl. Polym. Sci. 15, 2007–2021.

Costa, A., Macedonio, G., 2005. Viscous heating effects in fluids with temperature-dependent viscosity: triggering of secondary flows. J. Fluid Mech. 540. doi:10.1017/S0022112005006075.

Costa, A., Macedonio, G., 2003. Viscous heating in fluids with temperature-dependent viscosity: implications for magma flows. Nonlinear Process. Geophys. 10, 545–555.

Costa, A., Melnik, O., Sparks, R.S.J., Voight, B., 2007. Control of magma flow in dykes on cyclic lava dome extrusion. Geophys. Res. Lett. 34. doi:10.1029/2006GL027466.

Dekruif, C.G., Vanlersel, E.M.F., Vrij, A., Russel, W.B., 1985. Hard-sphere colloidal dispersions-viscosity as function of shear rate and volume fraction. J. Chem. Phys. 83, 4717–4725.

Deubener, J., Bruckner, R., 1997. Influence of nucleation and crystallization on the rheological properties of lithium disilicate melt. J. Non-Cryst. Solids 209, 96–111.

Dingwell, D.B., 1996. Volcanic dilemma: flow or blow? Science 273, 1054–1055.

Einstein, A., 1906. Eine neue Bestimmung der Moleküldimensionen. Annalen der Physik 19, 289–306.

Eriksson, R., Hayashi, M., Seetharaman, S., 2003. Thermal diffusivity measurements of liquid silicate melts. Int. J. Thermophys. 24, 785–796.

Frost, H.J., Ashby, M.F., 1982. Deformation-Mechanism Maps. 11–17.

Garboczi, E.J., Snyder, K.A., Douglas, J.F., 1995. Geometrical percolation threshold of overlapping ellipsoids. Phys. Rev. 52, 819–828.

Giordano, D., Russel, J.K., Dingwell, D.B., 2007. Viscosity of magmatic liquids: a model for volcanology. Geophys. Res. Abstr. 9.

Hess, K.U., Dingwell, D.B., 1996. Viscosities of hydrous leucogranitic melts: a non-Arrhenian model. Am. Mineral. 81, 1297–1300.

Holtzman, B.K., Kohlstedt, D.L., Morgan, J.P., 2005. Viscous energy dissipation and strain partitioning in partially molten rocks. J. Petrol. 46, 2569–2592.

Kerrick, D.M., Jacobs, G.K., 1981. A modified Redlich–Kwong equation for H_2O, CO_2, and H_2O–CO_2 mixtures at elevated pressures and temperatures. Am. J. Sci. 281, 735–767.

Krieger, G.I., 1972. Rheology of monodispersed lattices. Adv. Colloid Interface Sci. 3, 111–136.

Kulkarni, K.M., Kalpakjian, S., 1969. A study of barreling as an example of free deformation in plastic working. J. Eng. Ind. 91, 743–754.

Lange, R.A., 1994. The effect of H_2O, CO_2 and F on the density and viscosity of silicate melts. In: Carroll, M.R., Holloway, J.R. (Eds.), Volatiles in magmas (Reviews in mineralogy, 30). Mineral. Soc. Am., Washington DC, pp. 331–369.

Lejeune, A.M., Bottiga, Y., Trull, T.W., Richet, P., 1998. Rheology of bubble-bearing magmas. Earth Planet. Sci. Lett. 166, 71–84.

Llewellin, E.W., Manga, A., 2005. Bubble suspension rheology and implications for conduit flow. J. Volcanol. Geotherm. Res. 143 (1–3), 205–217.

Lyon, M.K., 2001. Structure formation in moderately concentrated viscoelastic suspensions in simple shear flow. J. Rheol. 45, 881–890.

Melnik, O., 2000. Dynamics of two-phase conduit flow of high-viscosity gas-saturated magma: large variations of sustained explosive eruption intensity. Bull. Volcanol. 62, 153–170.

Melnik, O., Sparks, R.S.J., 1999. Nonlinear dynamics of lava dome extrusion. Nature 402, 37–41.

Papale, P., 2001. Dynamics of magma flow in volcanic conduits with variable fragmentation efficiency and nonequilibrium pumice degassing. J. Geophys. Res. 106, 11043–11065.

Papale, P., 1999. Strain-induced magma fragmentation in explosive eruptions. Nature 397, 425–428.

Papale, P., Neri, A., Macedonio, G., 1998. The role of magma composition and water content in explosive eruptions: 1. Conduit ascent dynamics. J. Volcanol. Geotherm. Res. 87, 75–93.

Papale, P., Moretti, R., Barbato, D., 2006. The compositional dependence of the saturation surface of H_2O+CO_2 fluids in silicate melts. Chem. Geol. 229, 78–95.

Paterson, M.S., Olgaard, D.L., 2000. Rock deformation tests to large shear strains in torsion. J. Struct. Geol. 22, 1341–1358.

Polacci, M., Papale, P., Del Seppia, D., Giordano, D., Romano, C., 2004. Dynamics of magma ascent and fragmentation in trachytic versus rhyolitic eruptions. J. Volcanol. Geotherm. Res. 131, 93–108.

Romano, C., Giordano, D., Papale, P., Mincione, V., Dingwell, D.B., Rosi, M., 2003. The dry and hydrous viscosities of silicate melts from Vesuvius and Phlegrean Fields. Chem. Geol. 202, 23–38.

Rosemberg, C.L., Handy, M.R., 2005. Experimental deformation of partially melted granite revisited: implications for the continental crust. J. Metamorph. Geol. 23, 19–28.

Rosi, M., Principe, C., Vecci, R., 1993. The 1631 Vesuvius Eruption — a reconstruction based on historical and stratigraphical data. J. Volcanol. Geotherm. Res. 58, 151–182.

Rutherford, M.J., Baker, L., Pallister, J.S., 1993. Experimental petrology applied to volcanic processes. Eos 74, 671.

Rutter, E.H., Brodie, K.H., Irving, D.H., 2006. Flow of synthetic, wet, partially molten "granite" under undrained conditions: an experimental study. J. Geophys. Res. 111. doi:10.1029/2005JB004257.

Ryerson, F.J., Weed, H.C., Piwinskii, A.J., 1988. Rheology of subliquidus magmas .1. picritic compositions. J. Geophys. Res. 93, 3421–3436.

Saar, M.O., Manga, M., Cashman, K.V., Fremouw, S., 2001. Numerical models of the onset of yield strength in crystal-melt suspensions. Earth Planet. Sci. Lett. 187, 367–379.

Sato, H., 2005. Viscosity measurement of subliquidus magmas: 1707 basalt of Fuji volcano. J. Mineral. Petrol. Sci. 100, 133–142.

Scott, T., Kohlstedt, D.L., 2006. The effect of large melt fraction on the deformation behavior of peridotite. Earth Planet. Sci. Lett. 246, 177–187.

Smith, W.E., Zukoski, C.F., 2004. Flow properties of hard structured particle suspensions. J. Rheol. 48, 1375–1388.

Thomas, D.G., 1965. Transport characteristics of suspension .8. A note on viscosity of Newtonian suspensions of uniform spherical particles. J. Colloid Sci. 20, 267–277.

Vanderwerff, J.C., Dekruif, C.G., 1989. Hard-sphere colloidal dispersions-the scaling of rheological properties with particles-size, volume fraction, and shear rate. J. Rheol. 33, 421–454.

Vedeneeva, E.A., Melnik, O., Barmin, A.A., Sparks, R.S.J., 2005. Viscous dissipation in explosive volcanic flows, Geophys. Res. Lett. 32. doi:10.1029/2004GL020954.

Webb, S.L., Dingwell, D.B., 1990. Non-Newtonian rheology of igneous melts at high stresses and strain rate: experimental results for rhyolite, andesite, basalt, and nephelinite. J. Geophys. Res. 95, 15695–15701.